Progress Report and Summary (July 1, 2006, to December 31, 2019)

to:

U.S. Department of Energy
Office of Science
Basic Energy Sciences Program

GRANT #DE-FG02-06ER15783

Udo Becker (Principal Investigator)
Rodney C. Ewing (Co-P.I. part of the time)

Department of Earth and Environmental Sciences
The University of Michigan, 2534 C.C. Little Building
1100 N. University Avenue, Ann Arbor, Michigan 48109-1005

phone: (734) 615 6894, fax: (734) 763 4690, e-mail: ubecker@umich.edu

Abstract

A topic that we addressed in the earlier part of this grant was **the radiation effects in minerals**. While radiation effects can be used in the Earth sciences, for example, for dating exhumation rates, they are also important to understand the behavior of mineral-like crystalline phases under irradiation and if they would be good candidates as waste forms for radioactive materials. Therefore we have tested different materials in how they behave under different radiations. A uranyl-peroxide containing mineral, studtite, is expected to form as a consequence of α radiolysis of water in contact with spent nuclear fuel (SNF) in a geologic repository. Studtite was exposed to different fluences of radiation, and amorphization was analyzed as a function of these doses. In a different set of experiments, two other uranium -containing minerals, soddyite and uranophane, were studied under electron irradiation and over the temperature range of 25-300 °C. Under certain conditions the formation of nanocrystalline $U0_2$ was observed. Related to this we synthesized different uranium -containing compounds, for example, coffinite, $USiO_4$, has been produced by hydrothermal synthesis and was analyzed using different electron microscopy and diffraction methods. Related to this, phosphorous-rich coffinite, $U(Si,P)O_4{\cdot}H_2O$, from the natural nuclear reactor at Bangombe, Gabon, has been examined as an important primary mineral and alteration product of uraninite under reducing conditions. In addition, a mineral assemblage of coffinite, $USiO_4{\cdot}nH_2O$, carbonate-fluorapatite and (Ca, Sr)-(meta)autunite from the Woodrow Mine, Grants uranium region, New Mexico, has been investigated in order to understand the influence of a P-rich micro-geochemical environment on precipitation of coffinite and its subsequent alteration under oxidizing conditions. Finally, the response of synthetic coffinite to energetic ion beam irradiation was investigated.

The second complex topic was the mechanism of **redox reactions of actinides**, with special emphasis on the kinetics. This topic led to the development of computational and experimental techniques to approach the redox mechanism in a more fundamental way, specifically to conceptualize a standard set of kinetic roadblocks that could be built into a more fundamental kinetic theory that is less based on a black-box model. Here, we have combined experimental techniques such as electrochemistry, electrochemical atomic force microscopy, x-ray photoelectron and Auger spectroscopy, electron microscopy, and a new set of quantum mechanical calculations that allow for the derivation of reaction paths. In addition, the role of mineral surfaces was evaluated in catalyzing reactions as they might be doing it in natural environments, and geologic barriers, but also in the near field of nuclear waste repositories. In addition, we have developed an experimental setup to quantify the synergistic interaction of different organic ligands as e^- donors and TiO_2 as a photocatalyst, with light at different wavelengths, for uranyl reduction, showing that all components are necessary for efficient photoreduction. In addition, electronic and atomic structure, thermodynamics, and reaction pathways were investigated for light -induced redox reactions.

The third complex topic developed in the grant period was the **incorporation of actinide ions into minerals as well as actinide metal organic frameworks**. Step by step, we have developed a more comprehensive picture of the incorporation energies, structures, and electronic properties of actinyls incorporated into sedimentary minerals, such as carbonates and sulfates, iron oxides that, in addition to being present in natural environments, maybe a corrosion product of nuclear waste containers**,** and jarosites that are common waste products in acid mine setting s and also occur in uranium mines. There is also a progression of theoretical concepts within this series of papers: while our earlier papers **l**ay the ground rules for combining aqueous ions and periodic minerals within the same chemical equation (typically a roadblock for traditional quantum-mechanical models), and we have extended the usage of endmember minerals by complex solid solutions series on the cation and anion sites. Furthermore, while typically only equilibria between dissolved species and incorporation into bulk minerals are considered, our latest contribution analyzes the thermodynamics along the entire reaction path from solution, to surface adsorption, to incorporation into the uppermost surface layer, and finally to incorporation into the bulk solid.

Table of Contents

1 Summary of topics and achievements 4

1.1 Radiation effects in minerals 4

1.1.1 Stability of uranium(VI) peroxide hydrates under ionizing radiation. 4

1.1.2 The effects of ionizing radiation and temperature on uranyl silicates: soddyite $(UO_2)_2(SiO_4)(H_2O)_2$ and uranophane $Ca(UO_2)_2(SiO_3OH)_2{\cdot}5H_2O$ 4

1.2 Synthesis and physicochemical properties of actinide-containing silicates 4

1.1.1 Synthesis and characterization of coffinite 4

1.2.1 Structure and chemical composition of P-coffinite from natural fission reactor at Bangombé, Gabon 5

1.2.2 Precipitation and alteration of coffinite ($USiO_4{\cdot}\,nH_2O$) in the presence of apatite. 5

1.2.3 Response of synthetic coffinite to energetic ion beam irradiation. 7

1.3 Redox processes 7

1.3.1 *In situ* AFM Investigation of U(VI) reduction by Fe(II) on hematite surfaces 7

1.3.2 Electrochemistry and redox potentials, experimental and theoretical 7

1.3.3 Principles of homogeneous reaction kinetics 9

1.3.4 Photo-(electro)-chemistry 10

1.4 Incorporation of actinyls into mineral surfaces, solid solutions 10

1.4.1 Neptunium incorporation into uranium alteration phases 10

1.4.2 Np-incorporation into uranyl phases: A quantum-mechanical evaluation 11

1.5 Thermodynamic properties of actinide-containing solid solutions 12

1.5.1 Simulation of thermodynamic mixing properties of actinide-containing zircon solid solutions 12

1.6 Metal-organic frameworks (MOFs), their thermodynamics, and potential for actinide separation 13

1.7 Review Articles 14

1.7.1 Evolution of uranium and thorium minerals 14

1.7.2 Environmental impact of the nuclear fuel cycle: Fate of actinides 15

2 Publications that have come out of the support from this grant 15

1 Summary of topics and achievements

1.1 Radiation effects in minerals

While radiation effects can be used in the Earth sciences, for example, for dating exhumation rates, they are also important to understand the behavior of mineral-like crystalline phases under irradiation and if they would be good candidates as waste forms for radioactive materials. Therefore we have tested different materials in how they behave under different radiations.

1.1.1 Stability of uranium(VI) peroxide hydrates under ionizing radiation.

The uranyl peroxide, studtite, $[(UO_2)O_2(H_2O)_2]\cdot 2(H_2O)$ where O_2 indicates the peroxide group that is extremely rare in mineral, is expected to form as a consequence of α radiolysis of water in contact with spent nuclear fuel (SNF) in a geologic repository. Investigation of its stability is, therefore, of critical importance because secondary U(VI) phases may incorporate trace amounts of radionuclides and thus retard their mobility away from a repository site. To examine the effect of ionizing radiation on uranyl peroxides, electron-beam irradiation experiments have been conducted on two synthetic uranyl peroxides: studtite and metastudtite ($UO_4\cdot 2H_2O$) **[1]**. All experiments were done using a transmission electron microscope (TEM) with an acceleration voltage of 200 kV at room temperature. The fluence required to completely amorphize studtite was 0.51–1.54 × 10^{17} e/cm^2, which is equivalent to an absorbed dose of 0.73–1.43 × 10^7 Gy. Metastudtite becomes amorphous at a higher absorbed dose (1.31 × 107 Gy) than studtite, most likely because it contains fewer water molecules in its structure. These uranyl peroxides partially amorphize at doses that are one-tenth of the dose required for complete amorphization. With continued irradiation, uraninite nanocrystals form that are a few nanometers in diameter, at 4–20 × 10^{10} Gy. In a geologic repository, for spent nuclear fuel, the estimated absorbed doses due to ionizing radiation may be as high as 10^8–10^{11} Gy after 10^6 years. This dose is well in excess of doses in the laboratory experiments that caused the uranyl peroxides to become amorphous and decompose.

1.1.2 The effects of ionizing radiation and temperature on uranyl silicates: soddyite $(UO_2)_2(SiO_4)(H_2O)_2$ and uranophane $Ca(UO_2)_2(SiO_3OH)_2\cdot 5H_2O$

The stability of soddyite under electron irradiation has been studied over the temperature range of 25-300 °C **[2]**. At room temperature, soddyite undergoes a crystalline-to-amorphous transformation (amorphization) at a total dose of 6.38 x 10(8) Gy. The electron-beam irradiation results suggest that the soddyite structure is susceptible to radiation-induced nanocrystallization of UO_2. The temperature dependence of amorphization dose increases linearly up to 300 °C. A thermo-gravimetric and calorimetric analysis (TGA-DSC) combined with X-ray diffraction (XRD) indicates that soddyite retains its water groups up to 400 °C, followed by the collapse of the structure. Based on the thermal analysis of uranophane, the removal of some water groups at relatively low temperatures provokes the collapse of the uranophane structure. This structural change appears to be the reason for the increase of amorphization dose at 140 °C. According to the results obtained, the radiation field of a nuclear waste repository, rather than temperature effects, may cause changes in the crystallinity of soddyite and affect its stability during long-term storage.

1.2 Synthesis and physicochemical properties of actinide-containing silicates

1.1.1 Synthesis and characterization of coffinite

Coffinite, $USiO_4$, has been produced by hydrothermal synthesis. The synthesis products, coffinite nanoparticles (50 nm in size) with UO_2 nanoparticles (a few nanometers), are always associated even if they are not always detected by XRD measurements **[3, 4]**. The formation of coffinite was shown to be very sensitive to several experimental parameters. The most important of these parameters are the pH, which must be in the range 8 to 9.5, the pressure, which must be below 50 bars, and the reaction conditions, which must be oxygen-free to maintain uranium in its tetravalent oxidation state. XRD and TEM reveal

that tetragonal coffinite accounts for more than 90% of the final products while the by-products UO_2 and a Si-rich amorphous phase are also present. The structural formula of the obtained coffinite is close to $USiO_4$, as determined using EMPA ($USiO_4$). XPS measurements show a peak chemical shift of the U-4f core levels by 1 eV toward higher binding energies in coffinite compared with stoichiometric UO_2. The U-4f(7/2) and U-4f(5/2) positions in coffinite are found to be near 380.8 ± 0.3 eV and 391.7 ± 0.3 eV, respectively.

1.2.1 Structure and chemical composition of P-coffinite from natural fission reactor at Bangombé, Gabon

Phosphorous-rich coffinite, $U(Si,P)O_4 \cdot H_2O$, from the natural nuclear reactor at Bangombe, Gabon (depth 12.25 m), has been examined as an important primary mineral and alteration product of uraninite under reducing conditions **[5-7]**. Based on electron microprobe analyses (EMPA) and textural relationships, two distinct types of coffinite have been identified: (1) P-coffinite- (i) [with P_2O_5 and $(REE+Y)_2O_3$ as high as 9.84 and 8.66 wt%, respectively] replaces uraninite and has a chemical formula of $(U_{0.84}Y,REE_{0.12}Ca_{0.10}Th_{0.003})\ (Si_{0.41}P_{0.34}\ S_{0.08})\ _5O_4$ and; (2) coffinite-(ii), lacks uraninite inclusions [with P_2O_5 and $(Y+REE)_2O_3$ up to 1.45 and 1.79 wt%, respectively] and has a chemical formula of $(U_{0.78}Ca_{0.05}Y,REE_{0.03}\ Th_{0.002})(Si_{1.02}P_{0.06})O_4$. The EMPA elemental maps reveal a homogeneous distribution of P, Si, Nd, and U in P-coffinite-(i). Charge-balance calculations indicate that S substitution for Si in the coffinite structure results in the enhancement of the incorporation of P and REEs. High EMPA totals (95.100 wt%), suggest that water is not an essential component of the coffinite structure. High-angle annular dark-field scanning transmission electron microscopy (HAADF-STEM) reveals the decomposition of single crystals of uraninite into 50 nm grains during the alteration process to P-coffinite-(i). High-resolution transmission electron microscopy (HRTEM) and selected area electron diffraction (SAED) patterns confirm that P-coffinite-(i) has the coffinite structure. However, P-coffinite-(i) has a large amorphous fraction, probably due to radiation damage caused by decay events. The calculated cumulative dose for both types of coffinite varies from $1.6.1.9 \cdot 10^{18}$ (α-decay events/mg), which is equivalent to 134.2-161.5 displacements per atom (dpa) that have accumulated most probably during the past 800 million years.

1.2.2 Precipitation and alteration of coffinite ($USiO_4 \cdot nH_2O$) in the presence of apatite.

A mineral assemblage of coffinite, $USiO_4 \cdot nH_2O$, n = 0-2, carbonate-fluorapatite (CFAp) and (Ca, Sr)-(meta)autunite (M-Aut) from the Woodrow Mine, Grants uranium region, New Mexico, has been investigated in order to understand the influence of a P-rich micro-geochemical environment on precipitation of coffinite and its subsequent alteration under oxidizing conditions **[5]**.

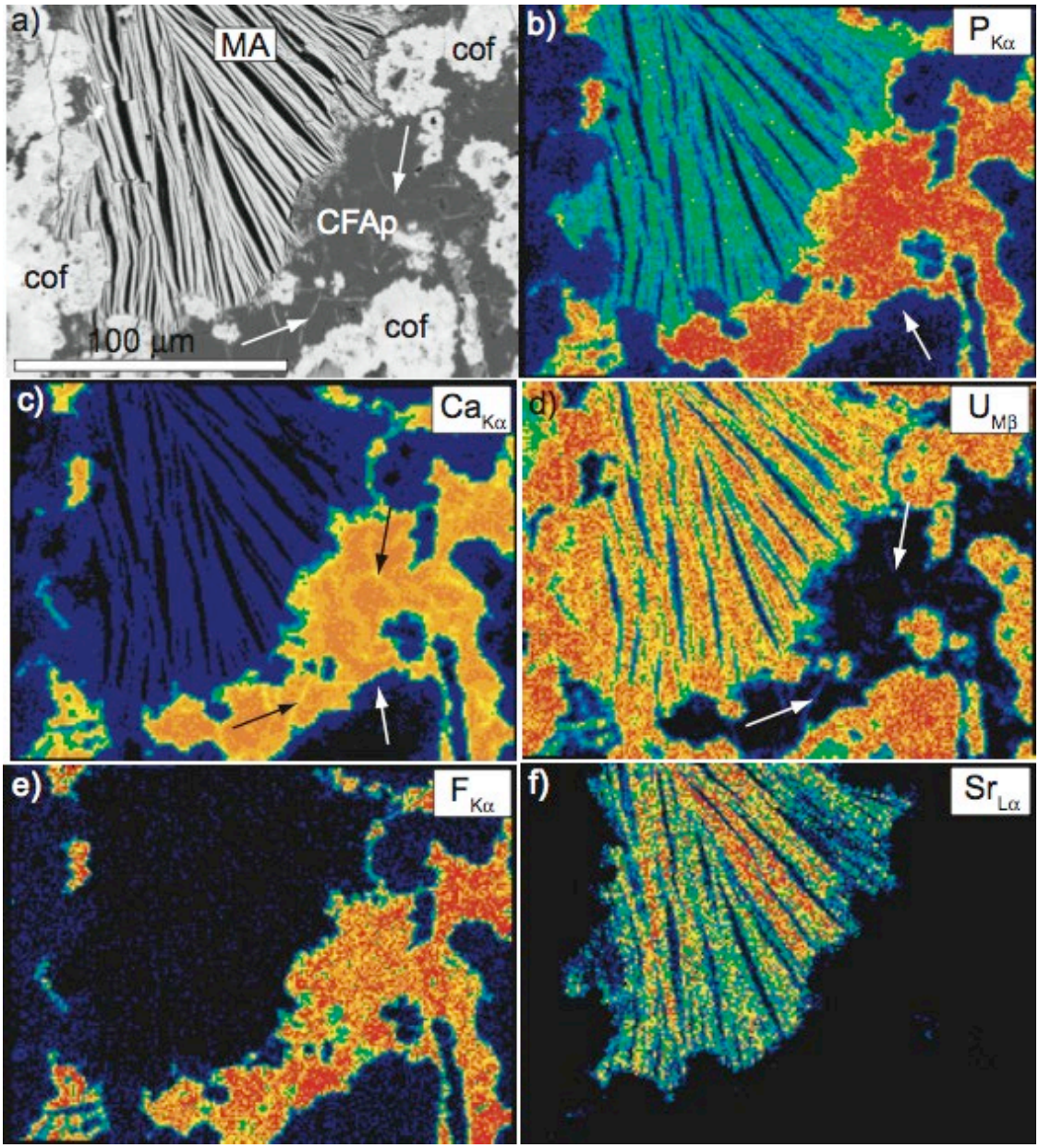

Figure 1. Elemental mapping of the associated coffinite, MA and CFAp; a) BSE image of the analyzed area; b) $P_{K\alpha}$; c) $Ca_{K\alpha}$; d) $U_{M\beta}$; e) $F_{K\alpha}$; f) $Sr_{L\alpha}$.

Fine-grained coffinite (≤10 µm) precipitated under reducing conditions replacing CFAp, pyrite and aluminosilicates. Electron-microprobe analyses (EMPA) of coffinite indicate limited incorporation of P_2O_5 and CaO, <2.7 and <3.0 wt%, respectively, into the coffinite structure during replacement of CFAp. The chemical formula of coffinite is $(U_{0.95}Ca_{0.15})$ $(Si_{0.84}P_{0.06})$. Analysis by high-angle annular dark-field scanning transmission electron microscopy (HAADF-STEM) revealed that coffinite initially formed as crystals as large as 100 nm at the edges of altered CFAp. Subsequently, the infiltration of (Na, Ba, Sr)-rich oxidizing fluids into fractures resulted in precipitation of Sr-rich M-Aut (up to 4 wt% of SrO) at the expense of coffinite and CFAp. High-resolution TEM reveals that Na-rich fluids caused a distortion of the ideal coffinite structure and stabilized amorphous domains that formed due to alpha-decay event radiation damage. Subsequently, the Na-enriched amorphous areas of coffinite were preferentially altered, and

secondary porosity formed at the scale of ≈1 μm. Porosity was formed during alteration of CFAp to M-Aut, which facilitated the migration of oxidizing fluids over distances of 150 μm into CFAp, as evidenced by precipitation of M-Aut. We report, for the first time, the precipitation of coffinite at the expense of apatite and the subsequent alteration of coffinite under P-rich, oxidizing conditions. These results show that micro-scale dissolution of apatite can create conditions conducive to the precipitation of U(IV)- and U(VI)-minerals, leading to the reduced mobility of U-species under both reducing and oxidizing conditions.

1.2.3 Response of synthetic coffinite to energetic ion beam irradiation.

Coffinite, USiO4, is one of the two most abundant and important naturally occurring U(4+) phases (the other is UO_2), and it is an alteration product of the UO_2 in spent nuclear fuel when in contact with silica-rich groundwater under reducing conditions. Despite its ubiquity, there are very limited data on the response of coffinite to radiation. **Lian et al. [4]** present the results of the first systematic investigation of energetic ion beam irradiation (1 MeV Kr^{2+}) of ultra-fine, synthetic coffinite (20-50 nm). In situ transmission electron microscopy (TEM) showed that the crystalline-to-amorphous transformation occurs at a relatively low dose at room temperature. The critical temperature, T_c, above which coffinite cannot be amorphized, is low. Synthetic coffinite is more stable as compared with isostructural zircon (ZrSiO4: T_c = 1000 K) and thorite (ThSiO4; T_c above 1100 K) upon ion beam irradiation at elevated temperature, suggesting enhanced defect annealing behavior in nano-sized synthetic coffinite. Irradiation was found to decrease the temperature required to induce phase-decomposition processes in coffinite upon thermal annealing. A good correlation among the critical amorphization temperature, T_c, phase decomposition temperature, T_f, and the temperature range of the two-phase (ZrO_2 and SiO_2) co-existed region was identified.

1.3 Redox processes

1.3.1 *In situ* AFM Investigation of U(VI) reduction by Fe(II) on hematite surfaces

The kinetics of uranyl (UO_2^{2+}) adsorption/reduction by ferrous iron has been studied at neutral pH, under anoxic and CO_2-free conditions. X-ray photoelectron spectroscopy confirms that hyperstoichiometric U_3O_8 precipitates on hematite reacted for 24 h in 160 μm uranyl nitrate and ferrous iron solution at pH 7.3 **[8]**. Moreover, *in situ* fluid tapping AFM experiments indicate a deceleration of the uranyl reduction rate within 24 h due to the existence of dominant orthorhombic U_3O_8 crystals. In addition, ferric oxide precipitates are formed during the first 5h, and schoepite appears after 5 h. Other applications of this technique can be found in **[9, 10]**

1.3.2 Electrochemistry and redox potentials, experimental and theoretical

1.3.2.1 The energetics and kinetics of uranyl reduction on pyrite, hematite, and magnetite surfaces: a powder microelectrode study

Many studies are describing the influence of parameters such as pH, pCO_2, and complexing ligands on the sorption of aqueous uranyl species on mineral surfaces. However, few of these studies attempt to describe the reduction reaction mechanisms and the factors that influence the rate of reduction, even though the oxidation state of uranium is the most important factor controlling the mobility of uranium. Reduction of aqueous U(VI) species results in the precipitation of insoluble uranium phases, which reduces its mobility in natural waters. In most cases, U(VI) reduction is kinetically inhibited unless a mineral surface or bacteria are present to catalyze the reaction. The role of mineral surfaces in catalyzing this reaction is poorly understood. There are a number of reasons for this: 1) these processes almost always involve a complex series of elementary reactions, each involving the transfer of one electron at a time, 2) it can be unwieldy to resolve the influence of individual environmental parameters in rate experiments (e.g., pH, pe, pO_2, concentration of other oxidants and reductants, other ions in solution, temperature, etc.), 3) it is challenging to differentiate rate constants for heterogeneous (surface) processes and homogeneous (solution) processes in order to assess the catalytic effects of the surface itself, and 4) rate-limiting processes such as electron

spin transitions have been widely ignored thus far. Our mineral surface group has developed an innovative electrochemical-based approach to address these challenges **[9-15]**.

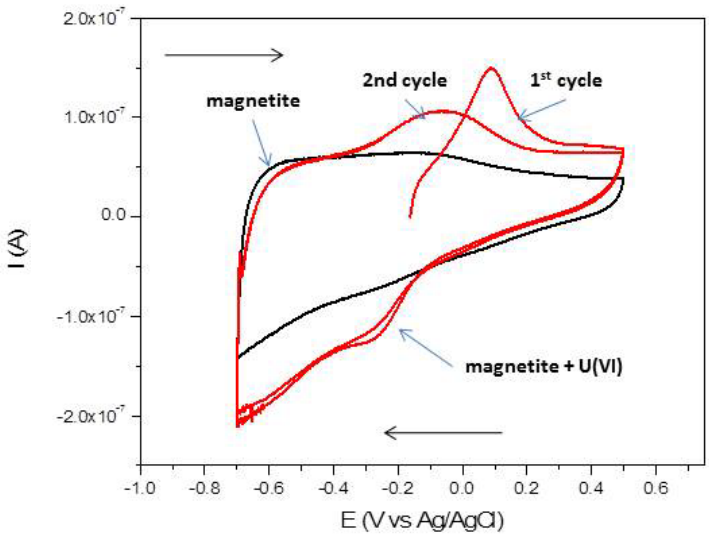

Figure 2: Voltammograms of magnetite in a uranyl-containing solution. The voltammogram shows a cathodic peak at ca. -0.25 V and a broad anodic peak similar to the anodic peak associated with U oxidation on pyrite. As in the case of pyrite, polarizing the magnetite electrode at -0.25 V for 5 minutes reveals a sharp peak at ca. +0.1 V on the first cycle that disappears on all subsequent cycles. This peak is most likely due to the oxidation of U(IV) phases on the surface that develop when a negative potential is applied to the electrode.

An electrochemical testing station has been constructed to evaluate U(VI) reduction (energetic and kinetics) on environmentally-important semiconducting minerals. Cyclic voltammetry using a powder microelectrode (PME) has been developed specifically to evaluate U(VI) reduction rates on pyrite (FeS_2), hematite (Fe_2O_3) and magnetite (Fe_3O_4, Fig. 2) under controlled conditions. PME enables rapid evaluation of redox kinetics and eliminates much of the variability inherent in electrochemical experiments using conventional electrodes fabricated from minerals. It should be noted that PME has not traditionally been applied to study environmental reactions, and demonstration of its advantages (e.g., electrochemical stability and rapid evaluation) in this study will provide the community with a new technique for evaluating other actinide-mineral reactions.

The voltammetric redox peaks of pyrite and hematite have been characterized by PME at pH 4 and pH 8, and the results are in agreement with redox peaks obtained using conventional electrodes. Pyrite lacks redox peaks between -0.6 and +0.5 V (vs Ag/AgCl). The initial results of our study show a voltammetric peak associated with the reduction/oxidation of U(VI) ↔U(V) on pyrite at ~0.22 V (vs. Ag/AgCl). This peak falls within the flat electrochemical window for pyrite and is dependent on the concentration of U(VI) in solution. To the authors' knowledge, this is the first time that the peak for U(VI) reduction on pyrite has been shown. Scan rate profiles for the U(VI) /U(V) redox couple have been obtained that will be used to determine kinetic parameters for reduction. Hematite shows a flat voltammetric profile that extends to ~-0.75 V (vs Ag/AgCl) before reduction of Fe(III) on the surface. In contrast to pyrite, hematite voltammetry shows no peak that could be attributed to the U(VI) /U(V) redox couple. However, after a conditioning step (i.e. the hematite electrode is held at sufficiently cathodic potentials to initiate the reduction of Fe(III) on the surface), a small U(VI) reduction peak appears at approximately the same potential as on pyrite. This result suggests that Fe(II) on the surface may be responsible for reduction of U(VI).

Once the electrochemical properties of the mineral powders exposed to U(VI) have been characterized by PME, the next step will be to visualize redox processes as they occur on primary cleavage or growth surfaces of sheet-structures. These processes will be directly imaged in electrolyte *(in situ)* using electrochemical scanning atomic force microscopy (AFM). X-ray photoelectron spectroscopy (XPS) will be employed evaluate the chemistry and oxidation state of redox product phases formed on the mineral surface.

Anodic and cathodic peaks corresponding to the 1 e^- reaction, U(VI)/U(V), were identified in cyclic voltammograms of pyrite, hematite, and magnetite at pH 4.5. A second oxidation peak, corresponding to the oxidation of U(IV), was identified on all mineral electrodes providing evidence for the formation of reduced uranium phases on the mineral surfaces. In addition, uranium-containing precipitates were identified on pyrite surfaces after polarization in a PME. High Tafel slopes (> 220 mV/dec on all minerals evaluated) suggest that uranyl reduction is mediated by insulating oxide layers that are present on the semiconducting mineral surfaces. The onset potential for uranyl reduction was determined for pyrite (>0.1 V vs. Ag/AgCl), and hematite and magnetite (between -0.02 and -0.1 V vs. Ag/AgCl). The onset potential values establish a baseline kinetic parameter that can be used to evaluate how solution conditions (*e.g.*, dissolved reductants, complexing ligands, and polarizing ions) affect the kinetics of uranyl reduction.

In addition, this study is the first attempt at using a PME, instead of a conventional mineral electrode, to evaluate redox processes on mineral surfaces. Stable and reproducible voltammograms obtained for pyrite, hematite, and magnetite were obtained with minimal electrode preparation. The results of this study demonstrate the feasibility of using PME's to evaluate redox energetics, kinetics, and mechanisms for other environmentally-relevant, mineral-solute systems. **Gebarski and Becker [11]** is the first electrochemical and computational study that applies electrochemistry to uranyl U_{60} nanoclusters. It shows the switching of the redox state of U within the cluster is possible, and to a certain degree reversible, between the (VI) and (V) oxidation states. In addition, oxidation state switching is observed on uranyl adsorbed to the nanoclusters, and its thermodynamics and kinetics are quantified using a combination of electrochemistry and quantum mechanical calculations.

Kim et al. [9] explore how semiconducting solids, such as magnetite (Fe_3O_4) and ilmenite ($FeTiO_3$), can facilitate otherwise-slow (for homogeneous reactions in solution) electron transfer (ET) between a reductant and oxidant as these species are adsorbed on their surfaces. This is a rare application of in situ electrochemical atomic force microscopy that allows for imaging of redox-dependent processes as they occur at a nanoscale.

Arumugam and Becker [16-18] are theoretical studies that create a basis for understanding redox reaction catalysis by semiconducting minerals. In **[18],** we test different surface sites and find that there are high (corners and kinks) or intermediate spins (terraces) on these sites, which changes the catalytic properties of pyrite by orders of magnitude. Then **[17]** describes how uranyl (an oxidant) and organic (e.g., hydroquinone) or inorganic reductants create molecular orbitals near the Fermi level that can span the entire distance from the reductant through the mineral surface to the oxidant (>10 Å) to facilitate ET.

Arumugam and Becker [16] reviews approaches and **[9-11, 13, 15, 16]** calculate the position of electrochemical peaks, based on the results of a thermodynamic cycle derived from quantum mechanical principles and presents new examples where these principles have been applied. References to [10, 13, 15, 19] are experimental examples of Fe-oxide catalyzed actinyl redox reactions.

Taylor et al. [20, 21] investigate how the intrinsic chemical and electronic properties of mineral surfaces (Fe oxides) and their associated ET pathways influence the reduction of U(VI) by surface-associated Fe(II).

Taylor et al. [21, 22] are the first studies to theoretically quantify the kinetics of electron transfer using Marcus theory as catalyzed by mineral surface.

1.3.3 Principles of homogeneous reaction kinetics

Bender and Becker [23] describe a new rigorous fundamental approach to quantify the kinetics of sub-reactions in a redox process in a way that is not just a black-box study of kinetics but identifies intermediate roadblocks and can, therefore, be used in a much more predictive way than traditional kinetic studies. This study uses collision theory to model bulk solution diffusion and formation of outer-sphere complexes, outer- to inner-sphere complex (OSC-ISC) transition, ET with different spin configurations.

Building upon the method developed and applied to plutonyl hydrolysis complexes in **[23], [24]** characterizes the effect of carbonate ligands and **[25]** of EDTA complexation on actinyl redox reaction

kinetics. Both complex types slow down kinetics by orders of magnitude due to larger activation energies for the OSC-ISC transition and non-spontaneous ET. The corresponding experimental studies can be found in **[14]** for EDTA complexed uranyl and in **[12]** for carbonate-complexed one.

1.3.4 Photo-(electro)-chemistry

Bender et al. [26] is a photo-electrochemical approach to study the influence of UV photons on the kinetics of uranyl reduction and uraninite formation using powder microelectrode voltammetry with and without light.

Kim et al. [27] uses a different experimental setup and studies the interplay of different organic ligands as e^- donors and TiO_2 as a photocatalyst, with light at different wavelengths, for uranyl reduction, showing that all components are necessary for efficient photoreduction. In addition, electronic and atomic structure, thermodynamics, and reaction pathways are investigated.

1.4 Incorporation of actinyls into mineral surfaces, solid solutions

Step by step, we are developing a more comprehensive picture of the incorporation energies, structures, and electronic properties of actinyls incorporated into sedimentary minerals, such as carbonates and sulfates (plutonyl and neptunyl, **[28-32]**), iron oxides **[30]** that, in addition to being present in natural environments, maybe a corrosion product of nuclear waste containers**,** and jarosites that are common waste products in acid mine setting s and also occur in uranium mines **[33]**. There is also a progression of theoretical concepts within this series of papers: **[28, 29, 34]** lay the ground rules for combining aqueous ions and periodic minerals within the same chemical equation (typically a roadblock for traditional quantum-mechanical models), and **[28]** extends the usage of endmember minerals by complex solid solutions series on the cation and anion sites. Furthermore, while **[5, 28-30, 32-35]** only consider the equilibrium between dissolved species and incorporation into bulk minerals, **[31]** analyzes the thermodynamics along the entire reaction path from solution, to surface adsorption, to incorporation into the uppermost surface layer, and finally to incorporation into the bulk solid.

1.4.1 Neptunium incorporation into uranium alteration phases

1.4.1.1 Quantum-mechanical evaluation of Np-incorporation into studtite

Radionuclide incorporation into the alteration products of corroded UO_2 in used nuclear fuel may control the release and mobility of key radionuclides, such as the very long-lived minor actinide, (237)Np ($\tau_{1/2}$ = 2.1 Ma). Studtite, $[UO_2(O_2)(H_2O)_2](H_2O)_2$, may form in the presence of peroxide produced by radiolysis of water in contact with the spent fuel. Experiments have indicated that the studtite structure can incorporate Np; however, due to the low concentrations in the solid, the incorporation mechanism could not be determined. In this study [28, 29, 34], density functional theory is used to calculate an optimized structure, determine the electronic density of states, and calculate the energetics of the incorporation of Np^{6+} vs. Np^{5+}+H^+ into the studtite structure. The definition of the source/sink phase (reference phase) for the cations involved in the incorporation process greatly affects the final incorporation energy. The incorporation energy of Np into studtite based on the 4+ oxide reference phases (e.g., source/sink = NpO_2/UO_2) results in lower incorporation energies (-0.07 and 0.63 eV for Np^{6+} and Np^{5+} incorporation, respectively) than the incorporation energy calculated using higher-oxide reference phases (e.g., Np_2O_5/UO_3), where the incorporation energies for Np^{6+} and Np^{5+} into studtite are 0.42 and 1.12 eV, respectively. In addition, Np^{6+}-incorporation into studtite is energetically more favorable than Np^{5+}-incorporation as assessed from the lower incorporation energy. Estimates of the solid-solution behavior from a combination of quantum-mechanical calculations and Monte-Carlo simulations indicate that the Np^{6+}- and U^{6+}-studtite solid solution is completely miscible at room temperature compared to a hypothetical Np^{6+}-studtite structure. The Np-studtite structure was calculated to be stable with respect to the corresponding oxides, but its formation may be kinetically hindered. Knowledge of the electronic structure provides insight into Np-bonding in the

studtite structure. The Np 5f orbitals are within the bandgap of studtite, which results in the narrow bandgap of Np-incorporated studtite (1.09 eV), as compared with the bandgap of studtite alone (2.29 eV).

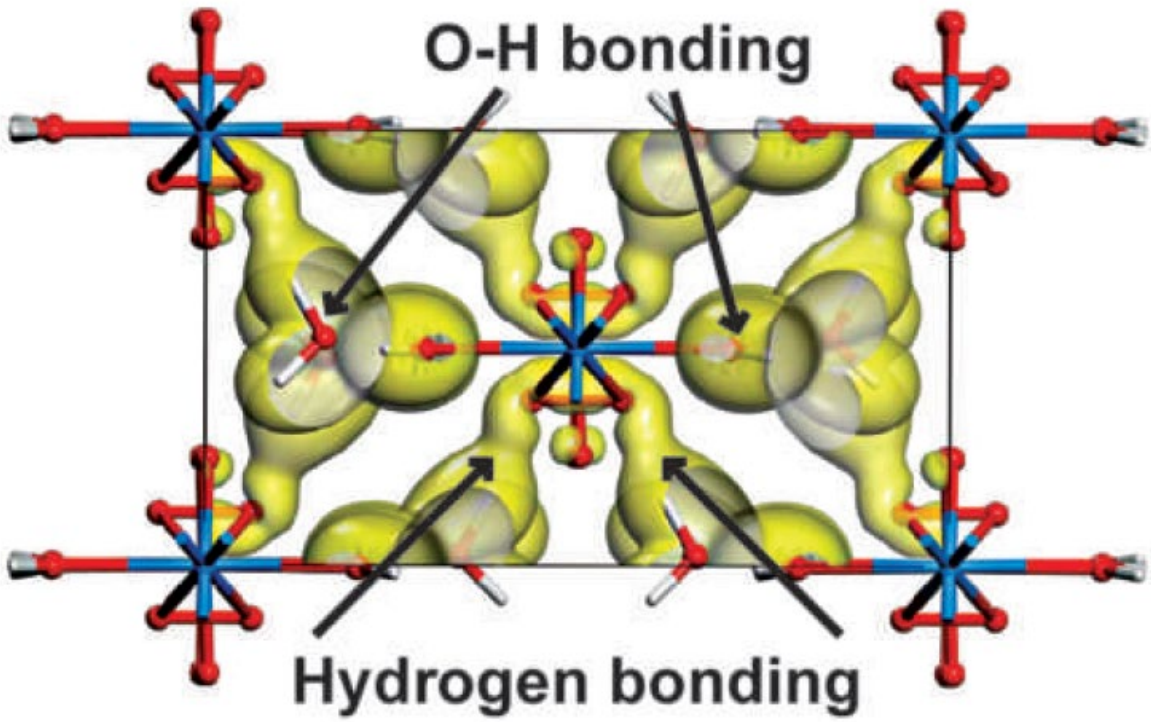

Figure 3. Electron density orbital projection between –8 and –6 eV showing O-H bonding in water molecules as well as hydrogen bonding between the water molecules and uranyl polyhedra.

The strength of this paper is that it combines the information of the band and electronic structure with deriving the (so far unknown) H positions in studtite (Fig. 3) and uses the information to deduce and quantify a mechanism for coupled substitution of Np^{5+} and H^{+} for U^{6+}. This allows for an estimate of the incorporation limit for this substitution process; furthermore, and this is new as well, the thermodynamics of substitution was calculated from quantum-mechanical principles as a function of the source phase of Np and the sink phase of U.

1.4.2 Np-incorporation into uranyl phases: A quantum-mechanical evaluation

Density functional theory calculations are used to compare mechanisms of charge-balanced Np^{5+}-incorporation into boltwoodite $[K(UO_2)(SiO_3OH)(H_2O)_{1.5}]$ **[34]**. The charge-balancing mechanisms considered include: *i*) H^{+} addition ($Np^{5+} + H^{+} \leftrightarrow U^{6+}$), *ii*) interlayer substitution ($Np^{5+} + Ca^{2+}/Mg^{2+} \leftrightarrow U^{6+} + K^{+}$), and *iii*) intra-layer substitution ($Np^{5+} + P^{5+} \leftrightarrow U^{6+} + Si^{4+}$). The choice of the source (of Np) and sink (of substituted cations) phases, the reference phases, for the cations involved in the incorporation reaction greatly affects the final calculated incorporation energy (ΔG_{rxn}). The incorporation energies using oxide (ΔG_{rxn} = 2.4 eV) and silicate (ΔG_{rxn} = 1.2 eV) reference phases are compared for the interlayer substitution mechanism. Since both the source of Np in environmental systems and the cations released are typically aqueous complexes, combinations of cluster and periodic simulations were employed to model exchange with aqueous complexes. For the H^{+} addition mechanism, incorporation from oxides reference phases (ΔG_{rxn} = 0.79 eV) is less favorable than from aqueous (ΔG_{rxn} = 0.66 eV) reference species. Estimates of the solid-solution behavior of Np^{5+}/P^{5+}- and U^{6+}/Si^{4+}-boltwoodite solid solutions are used to predict the limit

of Np-incorporation into boltwoodite, where the ΔG_{rxn} of 0.86 eV results in a maximum amount of incorporation of 768 ppm at 300 °C.

Table 1
Stoichiometric reactions describing the coupled substitution of Np^{5+} and H^+ for U^{6+} in boltwoodite comparing the Np-oxide source phases and U-oxide sink phases.

	Reactants	↔	Products	ΔE_{rxn} (kJ/mol)
Substitution mechanism I: $Np^{5+} + H^+ \leftrightarrow U^{6+}$				
1	Bolt + NpO_2 + 1/4 O_2 + 1/2 H_2O	↔	(bolt − U^{6+} + Np^{5+} + H^+) + UO_3	45.3
2	Bolt + 1/2 Np_2O_5 + 1/2 H_2O	↔	(bolt − U^{6+} + Np^{5+} + H^+) + UO_3	93.6
3	Bolt + NpO_2 + 1/2 H_2O	↔	(bolt − U^{6+} + Np^{5+} + H^+) + UO_2 + 1/4 O_2	225.8
4	Bolt + 1/2 Np_2O_5 + 1/2 H_2O	↔	(bolt − U^{6+} + Np^{5+} + H^+) + UO_2 + 1/2 O_2	273.1
5	Bolt + $NpO_2(H_2O)_5^+$ + H_3O^+	↔	(bolt − U^{6+} + Np^{5+} + H^+) + $UO_2(H_2O)_5^{2+}$ + H_2O	12.5
6	Bolt + $NpO_2(H_2O)_5^+$ + H^+	↔	(bolt − U^{6+} + Np^{5+} + H^+) + $UO_2(H_2O)_5^{2+}$	−534.5
Substitution mechanism II: $Np^{5+} + Ca^{2+}/Mg^{2+} \leftrightarrow U^{6+} + K^+$				
7	Bolt + 1/2 Np_2O_5 + MgO	↔	(bolt − U^{6+} − K^+ + Np^{5+} + Mg^{2+}) + UO_3 + 1/2 K_2O	222.9
8	Bolt + 1/2 Np_2O_5 + CaO	↔	(bolt − U^{6+} − K^+ + Np^{5+} + Ca^{2+}) + UO_3 + 1/2 K_2O	183.3
9	$K_2(UO_2)_2(SiO_3OH)_2(H_2O)_3$ + 1/2 Np_2O_5 + $CaAl_2Si_2O_8$ + SiO_2	↔	$KCa(UO_2)(NpO_2)(SiO_3OH)_2(H_2O)_3$ + UO_3 + $KAlSi_3O_8$ + 1/2 Al_2O_3	67.5
Substitution mechanism III: $Np^{5+} + P^{5+} \leftrightarrow U^{6+} + Si^{4+}$				
10	Bolt + 1/2 Np_2O_5 + 1/2 P_2O_5	↔	(bolt − U^{6+} − Si^{4+} + Np^{5+} + P^{5+}) + UO_3 + SiO_2	−104.2
11	Bolt + 1/2 Np_2O_5 + $AlPO_4$	↔	(bolt − U^{6+} − Si^{4+} + Np^{5+} + P^{5+}) + UO_3 + SiO_2 + 1/2 Al_2O_3	85.9
12	Bolt + 1/2 Np_2O_5 + 1/6 $Ca_{10}(PO_4)_6F_2$ + 3/2 Al_2O_3 + 2 SiO_2	↔	(bolt − U^{6+} − Si^{4+} + Np^{5+} + P^{5+}) + UO_3 + 1/6 CaF_2 + 3/2 $CaAl_2Si_2O_8$	−2.9

What is new in this paper is that the concept of source and sink phases has been carried a lot further by combining periodic solids and dissolved species in the same chemical equation where each species is derived from quantum-mechanical principles using different approaches. While this would normally be an inconsistent nightmare for every modeler, this was achieved by combining consistent chemical equations, using a consistent approach. The result is a big step forward in analyzing more realistic equilibria of environmentally-important adsorption-desorption reactions, as described in Table 1. In addition, a more complex model for entropy calculation as part of the thermodynamic integration of configurations enthalpies was derived, which takes into account the fact that the energy of the second substitute (H^+, interlayer cation, or tetrahedral cation) is dependent on the spatial relationship to the first substitute.

1.5 Thermodynamic properties of actinide-containing solid solutions

1.5.1 Simulation of thermodynamic mixing properties of actinide-containing zircon solid solutions

One of the major issues with actinides is the extent to which they can be incorporated into important structure types.

Solid solutions among zircon ($ZrSiO_4$, $I4_1/amd$) and zircon-structured orthosilicates $ASiO_4$ (A = Hf, Th, U, Pu, or Ce) are important to a wide variety of applications: nuclear materials, geochronology, and even electronic materials. The thermodynamic mixing properties of the following seven binary solid solutions were simulated using density functional theory followed by Monte Carlo modeling and thermodynamic integration: $(Zr,Hf)SiO_4$, $(Zr,Th)SiO_4$, $(Zr,U)SiO_4$, $(Zr,Pu)SiO_4$, $(Zr,Ce)SiO_4$, (Hf,Pu) SiO, and $(Th,U)SiO_4$, $ZrSiO_4$, and $HfSiO_4$ were found to form a nearly ideal solid solution, but the miscibility of the other solid solutions was limited to no more than 12 mol% of the substituting cation **[36]**. The binaries were ranked by extent of miscibility: $(Zr,Hf)SiO_4$ > $(Th,U)SiO_4$ > $(Zr,Pu)SiO_4$ > $(Zr,Ce)\ SiO_4$ > $(Hf,Pu)SiO_4$ > $(Zr,U)SiO_4$ > $(Zr,Th)SiO_4$. The extent of solid solution has been estimated for each binary. The end-members $PuSiO_4$, $CeSiO_4$, and $USiO_4$ were determined to be unstable relative to a mixture of $SiO_{2(quartz)}$ and crystalline PuO_2, $CeO_{2(ceramic)}$, or $UO_{2(uraninite)}$. Isostructural thorite ($ThSiO_4$) is calculated to be marginally stable, but its monoclinic polymorph, huttonite, which has the structure of monazite, is marginally unstable

relative to $SiO_{2(quartz)}$ and $ThO_{2(thorianite)}$ at 0 K. If thermodynamic equilibrium could be reached at low temperatures, exsolution textures would appear in most zircon solid solutions perpendicular to [001], but perpendicular to a linear combination of [100] and [010] in $(Hf,Pu)SiO_4$.

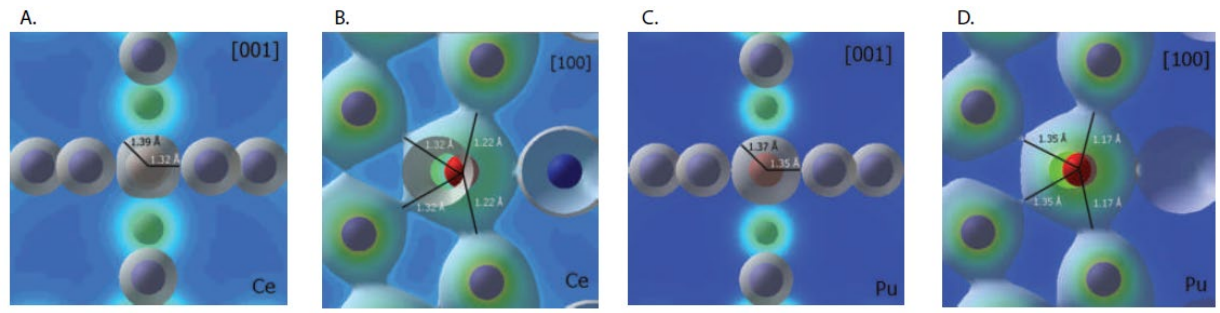

Figure 4: Charge density isosurfaces projected on (a) [001] for Ce, (b) [100] for Ce, (c) [001] for Pu, and (d) [100] for Pu. Plutonium and Ce (red) are coordinated by eight O atoms (blue). Plutonium appears to be more rounded than Ce in this structure, and the bonded ionic radius of Pu is slightly larger than that of Ce in the elongate O-cation bonds.

While this paper calculates the thermodynamic properties for a variety of actinide-containing solid solutions from atomistic principles, it compares results with more classical concepts such as ionic radius, and it analyzes the benefits and limitations of these older concepts. One such limitation is that actinide ions with their complex electronic structure are often not spherical (Fig. 4), which helps explain the Pu-Ce anomaly in terms of their thermodynamic solid solution behavior.

1.6 Metal-organic frameworks (MOFs), their thermodynamics, and potential for actinide separation

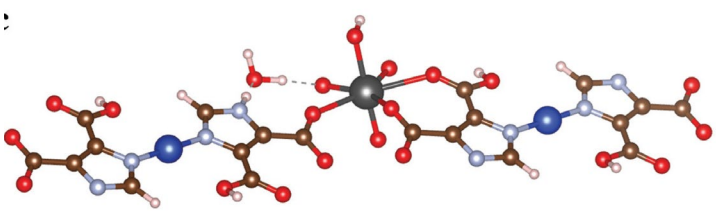

Structure of optimized coordination environment of Np^{5+}(dark grey) + H^+ incorporated U(azure)-MOF3

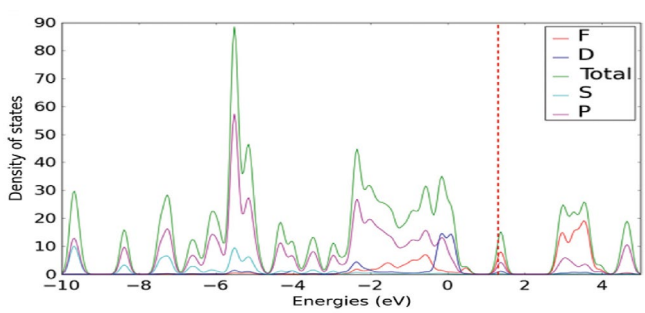

Figure 5. Structure of optimized coordination environment of Np5+(dark grey) + H+ incorporated U(azure)-MOF3

MOFs for actinides are a relatively new class of solids with largely unknown thermodynamic and electronic properties. While not necessarily envisioned to be used as industrial catalysts, they may control the kinetics of redox reactions of actinides in nuclear environments. The stability of uranium MOFs with different organic linkers was evaluated when U is replaced by Np(V and VI); subsequently, the ability of these mixed oxides was tested for the (photo)-catalysis of redox reactions. It was found that the coupled substitution of U^{6+} by Np^{5+} + H^+ from solution comes with a surprisingly low energetic cost (0.33 eV or more depending on the organic linker).

Incorporation of Np decreases the bandgap significantly. This first study of the electronic structure (band structure, DOS) of U- and Np-based MOFs may lead to design MOFs with specific optical or catalytic properties.

Our computational study **[37]** provides a detailed analysis of chemical bonding, charge distribution, geometric and electronic structural properties, and optical properties of actinide metal-organic frameworks

(MOFs) for the first time. The computational study **[35]** evaluates the relative stability and incorporation mechanism of Np into U-bearing MOFs, and therefore their potential for use as alternative media for actinide separation.

1.7 Review Articles

1.7.1 Evolution of uranium and thorium minerals

As part of a broad synthesis, R.C. Ewing, R.M. Hazen, and D.A. Sverjensky **[38]** have written a history of uranium and thorium minerals over the age of the Earth (Hazen et al., 2009). The purpose of this paper was to establish a context for understanding the very long-term behavior of actinides in geochemical cycles. The modes of accumulation and even the compositions of uraninite, as well as the multiple oxidation states of U (4+, 5+, and 6+), are a sensitive indicator of global redox conditions. In contrast, the behavior of thorium, which has only a single oxidation state (4+) that has very low solubility in the absence of aqueous F-complexes, cannot reflect changing redox conditions. The geochemical concentration of Th relative to U at high temperatures is therefore limited to special magmatic-related environments, where U^{4+} is preferentially removed by chloride or carbonate complexes and, at low temperatures, by mineral surface reactions.

Uranium and thorium's near-surface mineralogy provide a measure of a planet's geotectonic and geobiological history. In the absence of extensive magmatic-related fluid reworking of the crust and upper mantle, uranium and thorium will not become sufficiently concentrated to form their own minerals or ore deposits. Furthermore, in the absence of surface oxidation, all but a handful of the known uranium minerals are unlikely to form.

The origins and near-surface distributions of about 250 known uranium and/or thorium minerals elucidate the principles of mineral evolution. This history can be divided into four phases. The first, from similar to 4.5 to 3.5 Ga, involved successive concentrations of uranium and thorium from their initial uniform trace distribution into magmatic-related fluids from which the first U^{4+} and Th^{4+} minerals uraninite (ideally UO_2), thorianite (ThO_2), and coffinite ($USiO_4$), precipitated in the crust. The second period, from similar to 3.5 to 2.2 Ga, saw the formation of large low-grade concentrations of detrital uraninite (containing several wt% Th) in the Witwatersrand-type quartz-pebble conglomerates deposited in a highly anoxic fluvial environment. Abiotic alteration of uraninite and coffinite, including radiolysis and auto-oxidation caused by radioactive decay and the formation of helium from alpha particles, may have resulted in the fort-nation of a limited suite of uranyl oxide-hydroxides.

Earth's third phase of uranium mineral evolution, during which most known U minerals first precipitated from reactions of soluble uranyl $(U^{6+}O_2)^{2+}$ Complexes, followed the Great Oxidation Event (GOE) at similar to 2.2 Ga and thus was mediated indirectly by biologic activity. Most uraninite deposited during this phase was low in Th and precipitated from saline and oxidizing hydrothermal solutions (100 to 300 °C) transporting $(UO_2)^{2+}$ chloride complexes. Examples include the unconformity- and vein-type U deposits (Australia and Canada) and the unique Oklo natural nuclear reactors in Gabon. The onset of hydrothermal transport of $(UO_2)^{2+}$ complexes in the upper crust may reflect the availability of $CaSO_4$-bearing evaporites after the GOE. During this phase, most uranyl minerals would have been able to form in the O_2-bearing near-surface environment for the first time through weathering processes. The fourth phase of uranium mineralization began similar to 400 million years ago, as the rise of land plants led to non-marine organic-rich sediments that promoted new sandstone-type ore deposits.

The modes of accumulation and even the compositions of uraninite, as well as the multiple oxidation states of U (4+, 5+, and 6+), are a sensitive indicator of global redox conditions. In contrast, the behavior of thorium, which has only a single oxidation state (4+) that has very low solubility in the absence of aqueous F-complexes, cannot reflect changing redox conditions. The geochemical concentration of Th relative to U at high temperatures is therefore limited to special magmatic-related environments, where U^{4+}

is preferentially removed by chloride or carbonate complexes and, at low temperatures, by mineral surface reactions.

The near-surface mineralogy of uranium and thorium provides a measure of a planet's geotectonic and geobiological history. In the absence of extensive magmatic-related fluid reworking of the crust and upper mantle, uranium and thorium will not become sufficiently concentrated to form their own minerals or ore deposits. Furthermore, in the absence of surface oxidation, all but a handful of the known uranium minerals are unlikely to have formed.

1.7.2 Environmental impact of the nuclear fuel cycle: Fate of actinides

The resurgence of nuclear power as a strategy for reducing greenhouse gas (GHG) emissions has, in parallel, revived interest in the environmental impact of actinides **[39-41]**. Just as GHG emissions are the main environmental impact of the combustion of fossil fuels, the fate of actinides, consumed and produced by nuclear reactions, determines whether nuclear power is viewed as an environmentally "friendly" source of energy In this article, we summarize the sources of actinides in the nuclear fuel cycle, how actinides are separated by chemical processing, the development of actinide-bearing materials, and the behavior of actinides in the environment At each stage, actinides present a unique and complicated behavior because of the 5*f* electronic configurations.

2 Publications that have come out of the support from this grant

1. Rey, A., S. Utsunomiya, J. Gimenez, I. Casas, J. de Pablo, and R.C. Ewing, *Stability of uranium (VI) peroxide hydrates under ionizing radiation.* American Mineralogist, 2009. **94**(2-3): p. 229-235.
2. Sureda, R., I. Casas, J. Gimenez, J. de Pablo, J. Quinones, J. Zhang, and R.C. Ewing, *Effects of ionizing radiation and temperature on uranyl silicates: Soddyite $(UO_2)_2(SiO_4)(H_2O)_2$ and uranophane $Ca(UO_2)_2(SiO_3OH)_2 \bullet 5H_2O$.* Environmental Science & Technology, 2011. **45**(6): p. 2510-2515.
3. Pointeau, V., A.P. Deditius, F. Miserque, D. Renock, U. Becker, J. Zhang, N. Clavier, N. Dacheux, C. Poinssot, and R.C. Ewing, *Synthesis and characterization of coffinite.* Journal of Nuclear Materials, 2009. **393**(3): p. 449-458.
4. Lian, J., J.M. Zhang, V. Pointeau, F.X. Zhang, M. Lang, F.Y. Lu, C. Poinssot, and R.C. Ewing, *Response of synthetic coffinite to energetic ion beam irradiation.* Journal of Nuclear Materials, 2009. **393**(3): p. 481-486.
5. Deditius, A.P., S. Utsunomiya, V. Pointeau, and R.C. Ewing, *Precipitation and alteration of coffinite ($USiO_4 \bullet nH_2O$) in the presence of apatite.* European Journal of Mineralogy, 2010. **22**(1): p. 75-88.
6. Deditius, A.P., S. Utsunomiya, M.A. Wall, V. Pointeau, and R.C. Ewing, *Crystal chemistry and radiation-induced amorphization of P-coffinite from the natural fission reactor at Bangombe, Gabon.* American Mineralogist, 2009. **94**(5-6): p. 827-836.
7. Deditius, A.P., S. Utsunomiya, and R.C. Ewing, *The chemical stability of coffinite, $USiO4 \cdot nH_2O$; $0 < n < 2$, associated with organic matter: A case study from Grants uranium region, New Mexico, USA.* Chemical Geology, 2008. **251**(1-4): p. 33-49.
8. Niu, J., *Master's Thesis*. 2011, University of Michigan.
9. Kim, J.Y., M.C. Marcano, S. Kim, and U. Becker, *Imaging the reduction of uranyl on Fe-bearing minerals surfaces using in situ electrochemical AFM.* Geochimica et Cosmochimica Acta, 2020, submitted.

10. Yuan, K., D. Renock, R.C. Ewing, and U. Becker, *Uranium reduction on magnetite: Probing for pentavalent uranium using electrochemical methods.* Geochimica et Cosmochimica Acta, 2015. **156**: p. 194-206.
11. Gebarski, B.B. and U. Becker, *Electrochemical analysis of the kinetics of oxidation/reduction reactions of the peroxide-containing mineral studtite in comparison to uranyl peroxide clusters (U_{60}).* Radiochimica Acta, 2020, submitted.
12. Marcano, M.C., Y. Wang, S. Kim, and U. Becker, *Effect of carbonate complexation on electrochemical redox reactions of uranyl catalyzed by pyrite surfaces.* submitting to ACS Earth and Space Chemistry (June 2020), 2020.
13. Renock, D., M. Mueller, K. Yuan, R.C. Ewing, and U. Becker, *The energetics and kinetics of uranyl reduction on pyrite, hematite, and magnetite surfaces: A powder microelectrode study.* Geochimica et Cosmochimica Acta, 2013. **118**: p. 56-71.
14. Wang, Y., M.C. Marcano, S. Kim, and U. Becker, *Effect of EDTA complexation on redox reactions of uranium mediated by pyrite surfaces: A combined electrochemistry and quantum-mechanical calculation study.* submitted to ACS Earth and Space Chemistry, 2020.
15. Yuan, K., E.S. Ilton, M.R. Antonio, Z.R. Li, P.J. Cook, and U. Becker, *Electrochemical and spectroscopic evidence on the one-electron reduction of U(VI) to U(V) on magnetite.* Environmental Science & Technology, 2015. **49**(10): p. 6206-6213.
16. Arumugam, K. and U. Becker, *Computational redox potential predictions: Applications to inorganic and organic aqueous complexes, and complexes adsorbed to mineral surfaces.* Minerals, 2014. **4**(2): p. 345-387.
17. Arumugam, K. and U. Becker, *Actinyl adsorption and reduction on pyrite surface: Insights from DFT calculations.* ACS Earth and Space Chemistry, 2020, submitted.
18. Arumugam, K., D. Renock, and U. Becker, *The basis for reevaluating the reactivity of pyrite surfaces: spin states and crystal field d-orbital splitting energies of bulk, terrace, edge, and corner Fe(II) ions.* Physical Chemistry Chemical Physics, 2019. **21**(12): p. 6415-6431.
19. Yuan, K., R.C. Ewing, and U. Becker, *Thermodynamic mixing properties of the UO_2-HfO_2 solid solution: Density functional theory and Monte Carlo simulations.* Journal of Nuclear Materials, 2015. **458**: p. 296-303.
20. Taylor, S.D., M.C. Marcano, K.M. Rosso, and U. Becker, *An experimental and ab initio study on the abiotic reduction of uranyl by ferrous iron.* Geochimica et Cosmochimica Acta, 2015. **156**: p. 154-172.
21. Taylor, S.D., U. Becker, and K.M. Rosso, *Electron transfer pathways facilitating U(VI) reduction by Fe(II) on Al- vs Fe-oxides.* Journal of Physical Chemistry C, 2017. **121**(36): p. 19887-19903.
22. Taylor, S.D., M.C. Marcano, and U. Becker, *A first principles investigation of electron transfer between Fe(II) and U(VI) on insulating Al- vs. semiconducting Fe-oxide surfaces via the proximity effect.* Geochimica et Cosmochimica Acta, 2017. **197**: p. 305-322.
23. Bender, W.M. and U. Becker, *Determining the kinetics of discrete aqueous redox reaction sub-steps using computational methods: Application to reactions of plutonyl ($PuO_2^{+/2+}$) with Fe^{2+}, Fe^{3+}, and hydroxyl radical ($^{\cdot}OH$).* American Journal of Science, 2018. **318**(9): p. 893-920.
24. Bender, W.M. and U. Becker, *Resolving the kinetics of individual aqueous reaction steps of actinyl (AnO_2^{+} and AnO_2^{2+}; An = U, Np, and Pu) tricarbonate complexes with ferrous iron and hydrogen sulfide from first principles.* Radiochimica Acta, 2020. **108**(3): p. 165-184.
25. Kim, S., M.C. Marcano, Y. Wang, and U. Becker, *Exploring the kinetics of actinyl-EDTA reaction with ferrous iron using quantum mechanical calculations.* submitting to ACS Earth and Space Chemistry (Mai 2020), 2020.
26. Bender, W.M., N.D. Hughes, and U. Becker, *Effect of incident ultraviolet light on manganese oxide redox processes.* submitting to Geochimica et Cosmochimica Acta (June 2020), 2020.

27. Kim, Y., M.C. Marcano, B.R. Ellis, and U. Becker, *Photocatalytic reduction of uranyl: Effects of organic ligands and UV light wavelengths.* American Journal of Science, 2018. **318**(9): p. 949-968.
28. Shuller, L.C., R.C. Ewing, and U. Becker, *Quantum-mechanical evaluation of Np-incorporation into studtite.* American Mineralogist, 2010. **95**(8-9): p. 1151-1160.
29. Shuller-Nickles, L.C., W.M. Bender, S.M. Walker, and U. Becker, *Quantum-mechanical methods for quantifying incorporation of contaminants in proximal minerals.* Minerals, 2014. **4**(3): p. 690-715.
30. Bender, W.M. and U. Becker, *Quantum-mechanical investigation of the structures and energetics of uranium and plutonium incorporated into the magnetite (Fe_3O_4) lattice.* ACS Earth and Space Chemistry, 2019. **3**(4): p. 637-651.
31. Gebarski, B.B. and U. Becker, *Quantum-mechanical determination of the incorporation of pentavalent plutonium into carbonate and sulfate minerals.* Geochimica et Cosmochimica Acta, 2020. **269**: p. 693-710.
32. Walker, S.M. and U. Becker, *Uranyl (VI) and neptunyl (V) incorporation in carbonate and sulfate minerals: Insight from first-principles.* Geochimica Et Cosmochimica Acta, 2015. **161**: p. 19-35.
33. Kim, Y., A.S. Wolf, and U. Becker, *Thermodynamic mixing properties of alunite supergroup minerals: Quantum-mechanical modeling and thermodynamic analysis of sulfate, chromate, selenate, phosphate, and arsenate solid solutions, as well as uranyl incorporation.* Geochimica et Cosmochimica Acta, 2019. **248**: p. 138-160.
34. Shuller, L.C., R.C. Ewing, and U. Becker, *Np-incorporation into uranyl phases: A quantum-mechanical evaluation.* Journal of Nuclear Materials, 2013. **434**(1-3): p. 440-450.
35. Saha, S. and U. Becker, *A first principles study of energetics and electronic structural responses of uranium-based coordination polymers to Np incorporation.* Radiochimica Acta, 2018. **106**(1): p. 1-13.
36. Ferriss, E.D.A., R.C. Ewing, and U. Becker, *Simulation of thermodynamic mixing properties of actinide-containing zircon solid solutions.* American Mineralogist, 2010. **95**(2-3): p. 229-241.
37. Saha, S. and U. Becker, *The effect of the aliphatic carboxylate linkers on the electronic structures, chemical bonding and optical properties of the uranium-based metal-organic frameworks.* RSC Advances, 2015. **5**(34): p. 26735-26748.
38. Hazen, R.M., R.C. Ewing, and D.A. Sverjensky, *Evolution of uranium and thorium minerals.* American Mineralogist, 2009. **94**(10): p. 1293-1311.
39. Ewing, R.C., W. Runde, and T.E. Albrecht-Schmitt, *Environmental impact of the nuclear fuel cycle: Fate of actinides.* MRS Bulletin, 2010. **35**(11): p. 859-866.
40. Utsunomiya, S., A.B. Kersting, and R.C. Ewing, *Groundwater nanoparticles in the far-field at the nevada test site: Mechanism for radionuclide transport.* Environmental Science & Technology, 2009. **43**(5): p. 1293-1298.
41. Novikov, A.P., S.N. Kalmykov, S. Utsunomiya, R.C. Ewing, F. Horreard, A. Merkulov, S.B. Clark, V.V. Tkachev, and B.F. Myasoedov, *Colloid transport of plutonium in the far-field of the Mayak Production Association, Russia.* Science, 2006. **314**(5799): p. 638-641.